Struct Multidisc Optim (2016) 53:1113–1127
DOI 10.1007/s00158-015-1375-0

INDUSTRIAL APPLICATION

High fidelity multidisciplinary design optimisation of an electromagnetic device

J. N. Stander[1] · G. Venter[1] · M. J. Kamper[2]

Received: 27 July 2015 / Revised: 8 September 2015 / Accepted: 9 November 2015 / Published online: 10 December 2015

Abstract The application of multidisciplinary design optimisation is mostly confined to bi-disciplinary systems such as fluid-structure interaction problems. High fidelity models of three disciplines involving electromagnetic-thermal-structural designs are rare. Here, the multidisciplinary optimisation of such a design is presented. The device comprises a C-shaped iron core and a single coil. The problem is decomposed using a monolithic multidisciplinary feasible architecture. The multidisciplinary analyses involve a single three-dimensional finite element mesh for transient non-linear electromagnetic, non-linear-static thermal, and linear-static structural models. During each multidisciplinary iteration the mesh is linearly morphed. A gradient based optimisation algorithm in combination with a multi-start routine is applied to the constrained mass minimisation problem. Multidisciplinary feasibility is ensured by convergence of a single coupling parameter i.e. air-gap deformation. In conclusion, some multidisciplinary optimisation, analyses, and decomposition considerations are discussed.

Research funded by the GreenFund, DBSA

✉ J. N. Stander
jstander@sun.ac.za

G. Venter
gventer@sun.ac.za

M. J. Kamper
kamper@sun.ac.za

[1] Department of Mechanical and Mechatronic Engineering, University of Stellenbosch, Private Bag X1, Matieland, 7602, South Africa

[2] Department of Electrical and Electronic Engineering, University of Stellenbosch, Private Bag X1, Matieland, 7602, South Africa

Keywords MDO · MDF · FEA · Electromagnetic-thermo-structural · Design · Gradient-based

1 Introduction

Multidisciplinary Design Optimisation (MDO) studies are on the increase, partly because of new multi-physics numeric models, the ever-growing computational capabilities, and ultimately the goal to eliminate design assumptions. Two classes of MDO architectures exist. Architecture describes the system or problem decomposition scheme which concerns disciplinary division and the hierarchical ordering of disciplinary subsystems, the coupling of such subsystems, the mesh management, and the nesting of optimisation algorithms. The first and common architecture class involves monolithic or single-level schemes (Cramer et al. 1994). These follow the conventional approach, that is, a single optimisation operation at system level. Examples of such schemes are: the All-At-Once (AAO), the Simultaneous ANalysis and Design (SAND), the Individual Disciplinary Feasibility (IDF) (Alexandrov and Lewis 2002), and the Multi-Disciplinary Feasibility (MDF) schemes. The second architecture class includes distributed decomposition schemes (Martins and Lambe 2013). Here, optimisation operations are at both subsystem and system levels (Lasdon 2002). In this class, problem decomposition involves a Concurrent Sub-Space Optimisation (CSSO) (Sobieszczanski-Sobieski 1989) or a Collaborative Optimisation (CO) scheme (Balling and Wilkinson 1997). These differ in the way that the interdisciplinary constraints are managed. When using CSSO, each disciplinary subproblem needs to satisfy its own constraints as well as the surrogate constraints of other disciplines.

The CO approach entails balancing disciplinary constraints and the target values of coupling functions.

The MDO architecture is not the optimisation algorithm. The latter is a separate routine that evaluates the objective function by searching/populating different design variable instances within the specified design space. There are two types of optimisation algorithms, namely local and global optimisation algorithms (Venter G 2010). These algorithms may be applied to constrained and unconstrained problems, where both infeasible and feasible designs need to be optimised. A local optimisation algorithm searches for a local optimum nearest to the initial variable values. This is done by calculating and evaluating gradients. Occasionally, depending on the problem and initial values, the local optimum may also be a global optimum.

A global optimisation algorithm find a near global optimum in a design space which may contain numerous local optima. Global optimisation algorithms include deterministic methods (Floudas and Gounaris 2009), stochastic methods (Fouskakis and Draper 2007) and heuristic methods (Vinkó T and Izzo D 2011). These algorithms are applied in initial system design studies, that is, finding the realm of feasible designs. Local optimisation algorithms in conjunction with a multi-start technique may also be applied to global optimisation problems (Cox et al. 2001). Here, a design of experiments is used to obtain the starting points. In general, optimisation algorithm selection guidelines for a single discipline optimisation problem is also applicable to MDO problems (Venter G 2010).

In literature, MDO examples that include three or more disciplines are rare, even more so, if Finite Element (FE) models are considered. Tri-disciplinary examples mostly involve lumped analytical models or a combination of analytical and FE models. Finite element based electrical MDO examples usually entail electromagnetic-thermal (Kreuawan et al. 2008), electromagnetic and electronic control (Hammadi et al. 2012) and electro-mechanical systems (Ammar et al. 2005; Tosserams et al. 2010). In such problems, the objectives are of a steady-state, single metric nature. Full numeric electromagnetic-thermo-structural MDO examples are not found in literature. However, examples of Multi-Disciplinary Analysis (MDA) of electromagnetic-thermo-structural do exist (Amrhein et al. 2013; Keysan et al. 2011). These examples comprise lumped analytic models for the calculation of disciplinary physics.

MDO of a three-dimensional electromagnetic-thermo-structural device using FE models is presented. This device may be described as an electromagnet. Its mass is to be minimised in accordance with electrical, thermal, and mechanical load constraints. This high fidelity constrained MDO problem may be considered as a possible benchmark.

The problem is decomposed applying two MDF schemes, a conventional and a compact version, respectively. In the compact MDF scheme the optimisation algorithm is directly coupled to the MDA operation, hence, no nested disciplinary feasibility loop at MDA level is used. This scheme simplifies the MDO problem setup and yields a reduced optimisation solution time. A gradient based optimisation algorithm in combination with a multi-start procedure is applied in both MDF schemes. The disciplinary models and discretisation simplifications prior to optimisation are discussed. This is followed by discussions on the decomposition, the disciplinary coupling, and the calculation of the baseline model. Lastly, the MDO results are presented.

2 C-shaped electromagnetic device

The device consists of a C-shaped laminated steel core and a single preformed wound coil, see Fig. 1. The preformed, epoxy Vacuum Pressure Impregnated (VPI) coil is tightly secured to the core. Coil and core are further electrically insulated with thin glass bonded mica tape. A slit in the core (i.e. air-gap) is located opposite the coil. Localised widening of the core section at the air-gap leads to a minimal magnetic stray flux. Connecting an alternating current supply of fixed amplitude to the coil excites an alternating magnetic field.

The coil conductor dissipates Joule losses leading to an increased coil temperature, which in turn increases its resistance. The magnetic flux established by the alternating field is mostly constricted to the iron core. Iron has a much

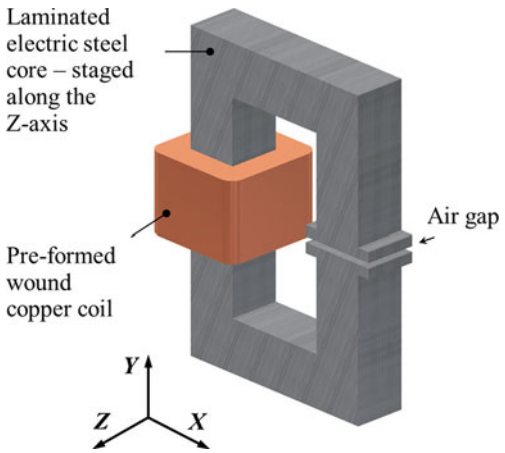

Fig. 1 Electromagnetic device with C-shaped core

higher magnetic permeability (ability to support flux) than air. Material non-linearities and iron hysteresis yield core losses which further heat up the device.

The magnetic flux produces magnetomotive forces at the air-gap which lead to magnetic stresses acting on the core surfaces. These stresses tend to close the air-gap. Structurally, the needed core dimensions are adjusted as to safely resist the air-gap stresses while maintaining a certain air-gap clearance. The important device performance metrics include its mass, the magnetic flux density distribution, its steady-state temperatures, and structural stresses. Other disciplinary design responses are the conductor diameter, the current density, the maximum magnetic flux in the core, the thickness of coil-core insulation, and the coil and core displacements.

3 Mesh

In MDO, two mesh management strategies exist: a common morphable mesh approach and a discipline-specific mesh approach. In the former, the number of nodes, the number of elements, and element types are kept constant across all disciplines. Mesh modification by linear morphing is applied since it is simple and fast. However, maintaining mesh quality and ensuring discipline compatibility are challenging. Therefore, element feasibility and mesh boundary checks need to be performed. In the discipline-specific mesh approach, each disciplinary model holds its own compatible mesh of specific element types, density, refinements and quality. During each MDA operation, changes in disciplinary boundary conditions are mapped and distributed to other disciplinary models. Critical regions are remeshed as to minimise discretisation errors.

In this study, the common morphable mesh approach was followed. The model is set in a Cartesian reference frame and is discretised with 33 012 linear tetrahedral elements. This element selection is governed by the electromagnetic code. This mesh is morphed as described in Section 5.1. Physical symmetry about the XY, XZ-planes allows model reduction to a quarter of the model (Fig. 2). These planes are defined as symmetry boundaries in the structural model, as natural boundaries in the thermal model, and as a symmetry and a natural boundaries in the electromagnetic model. In the latter, a natural boundary enforces a normal magnetic flux, and a symmetry boundary ensures a parallel flux.

In electromagnetic modelling, a coarse mesh with localised refinement is preferred (Pinchuk and Silvester 1985; Cros et al. 2011). Typically, the element characteristic length must equal the air-gap clearance, in near air-gap

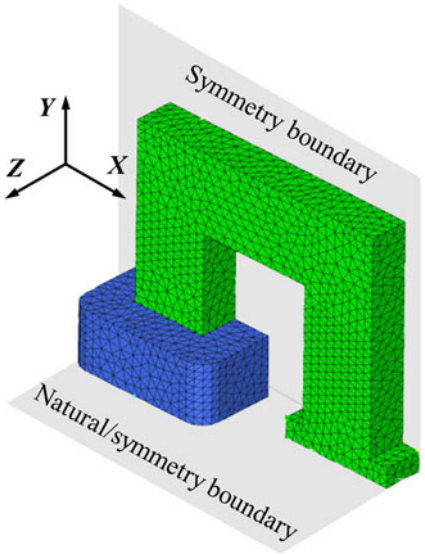

Fig. 2 Finite element - 1/4 model

regions. The number of elements selected is based on results of mesh dependency studies (Fig. 3). Morphing and element checks ensure that solution mesh independency is maintained.

Note that the disciplinary specific metrics are normalised. Only electromagnetic and structural parameters are considered. The mechanical stress metric does not converge due to poor element type and high stress concentrations caused by sharp geometric features. Thermal characteristics are not considered, because there exits no localised heat sources; in fact, both coil and core act as heat sources. The total amount of heat released equals the sum of Joule and iron losses.

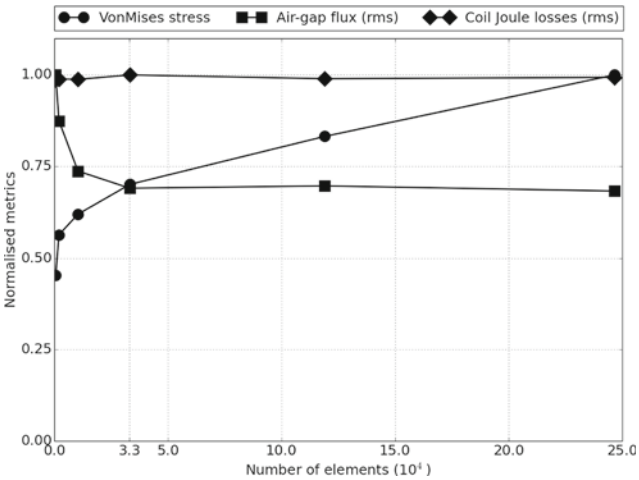

Fig. 3 Normalised mesh dependency study results

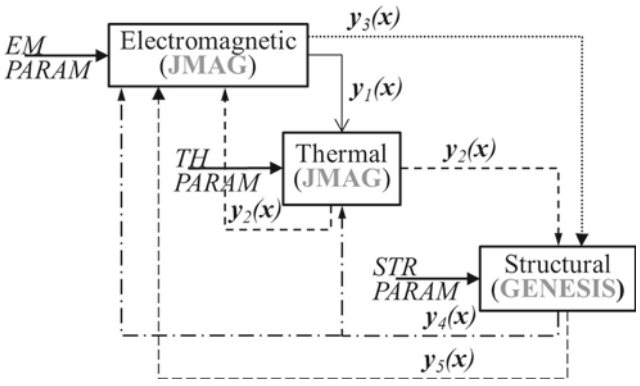

Fig. 4 The MDA hierarchy showing the discipline-couplings and FEA codes in brackets. $y_1(x)$ Joule/iron losses, $y_2(x)$ temperature field, $y_3(x)$ magnetic force field, $y_4(x)$ surface areas, $y_5(x)$ nodal displacements

Therefore, if the calculation of losses are based on mesh independent results, then the temperature distribution accuracy is acceptable.

4 Disciplinary models

The Finite Element Analyses (FEAs) of the Electro-Magnetic (EM), THermal (TH) and STRuctural (STR) models are performed applying commercial codes. Analyses follow a hierarchical order which is based on the functionality of the device. The MDA sequence starts with a transient EM analysis, followed by steady-state TH and linear-static STR analyses. These models are coordinated and coupled as illustrated in Fig. 4.

In the above, x denotes the design vector, $y_i(x)$ denotes the coupling variable vectors, and *PARAM* represents discipline state parameters, e.g. material properties. Discipline coupling involves the mapping and transferal of coupling vectors, such as: nodal coordinates, nodal displacements, electromagnetic forces, and nodal temperatures. The EM derived air-gap vector force field and Joule losses are passed to the STR and TH models, respectively. Nodal temperatures are included in the coil resistance and the thermal stress calculations. The nodal displacements are added to the existing mesh. The EM and STR FEA codes require different mesh formats. The mesh data are reformatted into different *NASTRAN* input formats (*.nas* and *.dat*) and *vice versa*. The *.nas* files only contain mesh data whereas the *.dat* files list all STR model properties as well as the morph vectors.

4.1 Electromagnetic model - EM

The EM model is created and analysed using the *JMAG v.13* multiphysics code (JMAG 2014). Its transient response is analysed applying an implicit solver. A complete cycle of 0.02 s is divided into 100 steps.

Electromagnetic, mechanical and thermal physical properties are sourced from literature or code catalogues for both copper (Cu95) and iron (Si-Fe M400-50A). Both electrical and magnetic material properties are temperature dependent. The magnetisation ability of the core depends on both its temperature (Takahashi et al. 2010; Cheng-Ju et al. 2014) and its mechanical stress state (Miyagi et al. 2010; Takahashi and Miyagi 2011). The temperature dependency of magnetic properties are ignored. Changes in the magnetisation (B-H) curve, magnetic permeability, magnetic hysteresis, and Joule losses within the temperature range of 20 °C to 100 °C are small, Cheng-Ju et al. (2014). Furthermore, the iron loss calculations do not incorporate the mechanical stress states. Data for such correlations are not readily available for the core material considered. The EM model is broken down into magnetic and electrical submodels. The magnetic FEA submodel calculation is based on the Maxwell equations (Pyrhönen et al. Wiley):

$$\nabla \times H = J + \frac{\partial D}{\partial t} \tag{1}$$

$$\nabla \times E = -\frac{\partial B}{\partial t} \tag{2}$$

$$\nabla \cdot D = \rho \tag{3}$$

$$\nabla \cdot B = 0 \tag{4}$$

where H, J, D, E, B, and ρ are the magnetic field strength, current density, electric flux density, electric field, magnetic field density, and electric change density, respectively. For real substances these equations are coupled by the constitutive equations

$$H = \frac{B}{\mu_0 \mu_r} \tag{5}$$

$$D = \varepsilon_0 \varepsilon_r E \tag{6}$$

where μ_0, μ_r, ε_0, and ε_r are the permeability of vacuum, relative permeability, permittivity of vacuum, and relative permittivity, respectively. Substituting (5) and (6) into (1) to (4) and introducing vector and scalar potentials A and ϕ as below

$$B = \nabla \times A \tag{7}$$

$$E = -\nabla\phi - \frac{\partial A}{\partial t} \tag{8}$$

one arrives at the coupled equation which links the magnetic and electrical submodels

$$\nabla \times \frac{1}{\mu_0 \mu_r} \times A = J - \sigma\left(\nabla\phi + \frac{\partial A}{\partial t}\right) - \varepsilon_0 \varepsilon_r \left(\nabla\phi + \frac{\partial A}{\partial t}\right). \tag{9}$$

Practically, the magnetic field analysis is based on a quasi-stationary approach in which the displacement current term $\varepsilon_0 \varepsilon_r (\nabla\phi + \frac{\partial A}{\partial t})$ is ignored.

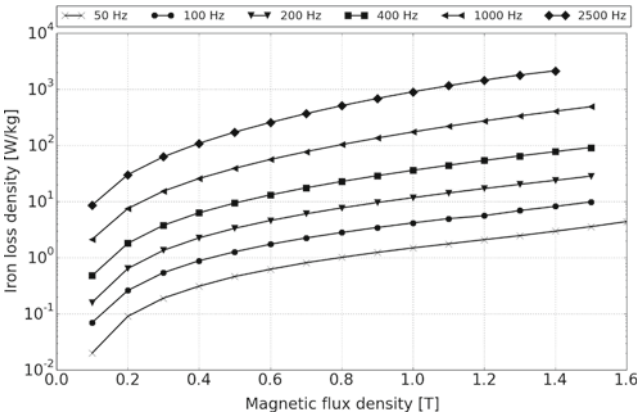

Fig. 5 M400-50A Si-Fe loss profiles at various frequencies and at 20 °C

Finally, the magnetic field for a finite element Ω is calculated with

$$\int_{\Omega}(\nabla \times \frac{1}{\mu_0 \mu_r} \times A - J + \sigma \frac{\partial A}{\partial t}) d\Omega = 0. \tag{10}$$

The air-gap flux density is obtained by solving (7) for the calculated magnetic vector potential. With the magnetic flux density and flux wave frequency known, the iron losses can be calculated. Iron losses comprise of Joule and hysteresis losses. Calculation of Joule losses involves the resistivity of iron. The iron losses and magnetic hysteresis curves at room temperature are represented in Fig. 5 and Table 1 JMAG (2014), respectively.

Material resistive properties at the initial temperature and at no mechanical stress are given in Table 2.

The electrical submodel, i.e. an equivalent electric circuit, comprises a current supply and a coil (Figs. 6a and b).

With reference to (10), the magnetic and electric submodels are coupled with a current density vector J

$$I = \int_s J \cdot n ds = \frac{1}{R_{coil}} (\Delta\phi - \int_{coil} (\frac{\partial A}{\partial t} \cdot c) dl) \tag{11}$$

Table 1 M400-50A Si-Fe hysteresis profile at 20 °C

B [T]	H [A/m]	B [T]	H [A/m]
0.0	0.0	1.0	113.2
0.1	32.6	1.1	137.8
0.2	43.5	1.2	180.2
0.3	50.8	1.3	269.5
0.4	57.2	1.4	516.8
0.5	63.4	1.5	1307.
0.6	69.9	1.6	3180.
0.7	77.3	1.7	6361.
0.8	86.0	1.8	10890.
0.9	97.2		

Table 2 Temperature specific material resistivities

Symbol	Property [Unit]	Value
Copper		
ρ_{cu_e0}	resistivity @ 20 °C [$\Omega \cdot$ m]	$1.68 \cdot 10^{-8}$
α_{cu_e}	coeff. of resistivity	0.0068
Si-Fe (M400-50A)		
–	laminate directionality	non-orientated
ρ_{fe_e0}	resistivity @ 20 °C [$\Omega \cdot$ m]	0.0042
α_{fe_e}	coeff. of resistivity	$6.51 \cdot 10^{-3}$

where I, R_{coil}, and $\Delta\phi$ are the supply current, the total coil resistance, and the difference in terminal potentials, respectively. The second right-hand term calculates the electromagnetic force induced by the oscillating magnetic flux. Coil resistance and inductance values specific to the FEM coil are calculated from the coil dimensions and number of turns. In turn, these depend on the conductor (wire) diameter.

A sinusoidal current with an amplitude of 20 A at 50 Hz is supplied. The number of conductor turns in the coil is fixed. With reference to Fig. 6b, the temperature dependent

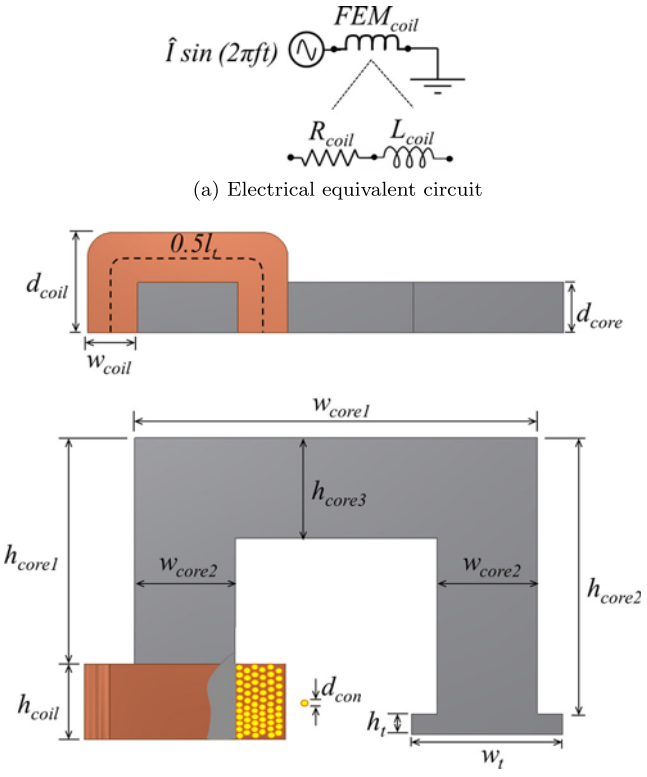

(a) Electrical equivalent circuit

(b) Model dimensions

Fig. 6 Electrical submodel

resistance of the coil is given by

$$A_{con} = \frac{k_{fill} w_{coil} h_{coil}}{N}, \quad d_{con} = \sqrt{A_{con}/\pi} \tag{12}$$

$$l_t = 2(w_{core} + w_{coil} + d_{coil} + d_{core}) \tag{13}$$

$$l_{con} = N l_t \tag{14}$$

$$\rho_{cu\_e/fe\_e}(T) = \rho_{cu\_e0/fe\_e0}(1 + \alpha_{cu\_e/fe\_e0}\Delta T) \tag{15}$$

$$R_c = \frac{\rho_{cu\_e} l_{con}}{A_{con}} \tag{16}$$

where A_{con}, d_{con}, l_t, and l_{con} are the conductor cross sectional area, wire diameter, average turn length, and total wire length, respectively.

Coil inductance is internally calculated in *JMAG*. Inductance is related to the energy stored in the magnetic field (Pyrhönen et al. Wiley)

$$W_\phi = \int_V \int_0^B H dB dV = \frac{1}{2} L i(t)^2 \tag{17}$$

where W_ϕ, L, and $i(t)$ are the magnetic energy, the coil inductance, and the current carried in a finite volume, respectively. Coil leakage inductance is nearly zero and therefore ignored.

4.2 Thermal model - TH

The device is immersed in quiescent air which is at a constant 20 °C and at atmospheric pressure. At these states air may be treated as an ideal gas. The heat generated (Joule losses) is passively transferred to the environment by means of natural convection. A maximum allowable operational temperature of 100 °C is specified. A non-linear steady-state thermal model is created in *JMAG*. Model simplifications involve neglecting the insulation caused by the small air-gaps between the iron laminates and between the coil and the core. Furthermore, heat transfer by radiation is also ignored because the device surface temperatures are below 100 °C. The equivalent thermal circuit applied is shown in Fig. 7. Note, the specific heat of components are included for the sake of completeness.

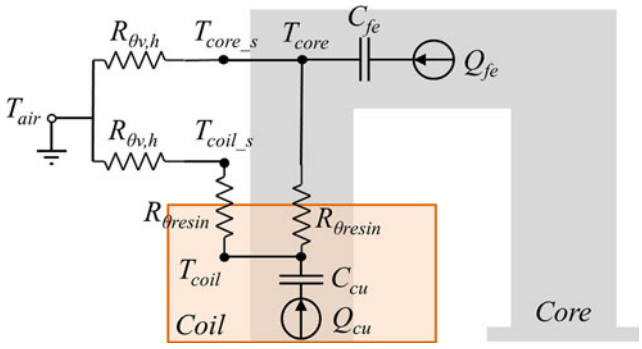

Fig. 7 Steady-state equivalent thermal circuit

The rms values of Joule (Q_{cu}) and iron losses (Q_{fe}) computed in the EM analyses are the heat sources. The temperature dependent conductivity coefficients (k_{cu}, k_{fe}, k_{air}) are linearly interpolated from tables given by Incropera and DeWitt (2002) as

$$k_{cu}(T) = 401.8 - 0.0821(T - 20.0) \tag{18}$$

$$k_{fe}(T) = 51.9 - 0.019(T - 20.0) \tag{19}$$

$$k_{air}(T) = 25.74 \cdot 10^{-3} + 0.075 \cdot 10^{-3}(T - 20.0) \tag{20}$$

where $T \in$ [20.0 °C, 127 °C],C, and k are in [J/kg·°C], and [W/m·°C], respectively. Thermal conduction resistance is calculated as

$$R_\theta = \frac{L}{kA} \tag{21}$$

where L, k, and A are the separation thickness, the thermal conductivity, and the area, respectively. The coefficient of thermal conductivity of the resin is constant. The TH model comprises two submodels. The first is limited to the FE domain. Here, material properties and boundary conditions are specified and applied to the FE model. This is followed by the internal coupling of the thermal and electromagnetic models. The second submodel includes external (environmental) thermal features such as convection. These features are included and linked in the FE model by means of a thermal equivalent circuit (Fig. 8). The circuit components, $FEM_{()}$, $R_{\theta v}$andR$_{\theta \mathrm{h}}$ present the FE model surfaces, and the calculated convection resistance for vertical and horizontal surfaces, respectively. Calculation of the convection resistances $R_{\theta v}$ and $R_{\theta h}$ includes correlations for the non-linear Rayleigh (Ra_L) and length averaged Nusselt ($\overline{Nu_L}$) numbers. Nusselt number correlation selection further distinguishes between vertical and horizontal heated surfaces.

The convection resistance for either core or coil, and vertical or horizontal surfaces are given by

$$R_{\theta v,h} = \left[\frac{1}{\overline{h_1} A_1} + \frac{1}{\overline{h_2} A_2} + \cdots + \frac{1}{\overline{h_n} A_n}\right]^{-1} \tag{22}$$

where $\overline{h_n}$ is the length averaged convection coefficient, which in turn is a function of the Nusselt number

$$\overline{h_n} = \frac{\overline{Nu_L} k}{L}. \tag{23}$$

The $\overline{Nu_L}$ numbers for vertical and horizontal surfaces, (24) and (25) respectively, are calculated as below. Note the

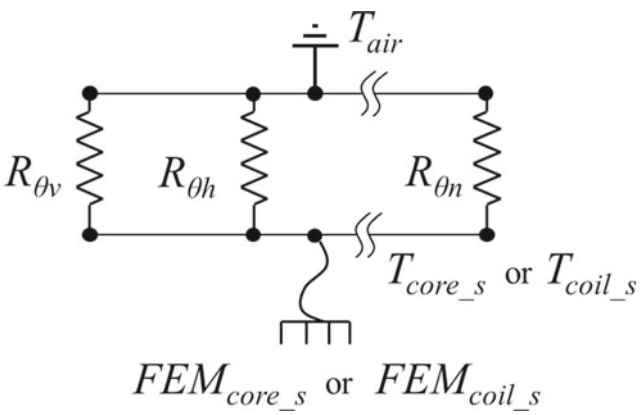

Fig. 8 Convention thermal circuit - parallel connected thermal resistances

Rayleigh number is constant as a laminar flow regime is assumed.

$$\overline{Nu_L} = 0.68 + 0.513 {Ra_L}^{0.25} \quad \forall \quad Ra_L \leq 10^9 \tag{24}$$

$$\overline{Nu_L} = 0.54 {Ra_L}^{0.25} \quad \forall \quad 10^4 \leq Ra_L \leq 10^9 \tag{25}$$

$$Ra_L = \frac{g\beta(T_s - T_{air})L^3}{\nu_{th\_air}(T_f)\alpha_{th\_air}(T_f)} \tag{26}$$

where $g, \beta, T_s, L, \nu_{th\_air}(T_f)$, and $\alpha_{th\_air}(T_f)$ are the gravitional acceleration, the expansion coefficient, the core or coil surface temperature, the characteristic length, the film temperature kinematic viscosity and thermal diffusivity, respectively. The temperature dependency of the two latter properties are approximated with linear interpolation functions derived from tables given by Incropera and DeWitt (2002). These functions are

$$\nu_{th\_air}(T_f) = 15.28 \cdot 10^{-6} - 0.104 \cdot 10^{-6}(T - 20.0) \tag{27}$$

$$\alpha_{th\_air}(T_f) = 21.83 \cdot 10^{-6} - 0.153 \cdot 10^{-6}(T - 20.0) \tag{28}$$

where both $\nu_{th\_air}(T_f)$, and $\alpha_{th\_air}(T_f)$ are in [m^2/s]. In an ideal gas, the expansion coefficient equals the reciprocal of its temperature in degree Kelvin. Characteristic length of a horizontal surface is approximated as the ratio between the surface area and surface perimeter. Core and coil film temperatures are given by

$$T_f = 0.5(T_s + T_{air}). \tag{29}$$

The above empirical equations are included in *JMAG* by means of *Python* scripting. Once these thermal parameters are known, the FE equation of the form

$$\kappa(T) \cdot T = Q + R(\nabla T) \tag{30}$$

is solved. Here κ, T, Q, and R are the temperature dependent coefficients, the nodal temperature field, the volumetric heat sources, and the heat fluxes, respectively.

4.3 Structural model - STR

A linear-static STR analysis is executed using the *GENESIS v13.1* code of Vanderplaats (2014). The model consists of two solid components: the laminated iron core, and the preformed copper coil. These bodies are discretised with linear tetrahedral elements (CTETRA). Separate PSOLID element properties are assigned to allow part distinction when analysing the EM model. Modified anisotropic (MAT9) and isotropic (MAT1) material properties are assigned to the core and coil, respectively. These are presented in Table 3.

The orthotropic material type is not native to *GENESIS*. This material is modelled by modifying an anisotropic material type (Mukundan 2003). The coil is a composite structure in which the copper conductor is formed and set within a resin. Oddly, no literature on structural coil modelling was found. With a resin-to-copper volume ratio is less than 20 % allows the coil to be modelled as a solid. The stiffening caused by the resin is ignored. The structural constraints and loads are allocated as shown in Fig. 9. The static linear-elastic problem solved is

$$K(\partial u + \partial u_T) = F_\delta + F_b \tag{31}$$

where, K, u, u_T, F_δ, and F_b are the global stiffness matrix, the structural deformation matrix, the thermal deformation matrix, and the structural load combination, respectively. The model stress field is calculated by

$$(\partial u + \partial u_T) = E^{-1}\sigma \tag{32}$$

Table 3 Structural material properties at 20 °C

Symbol	Property [Unit]	Value
Copper		
ρ_{cu}	density [kg/m^3]	8750.0
E_{cu}	modulus of elasticity [kN/mm^2]	132.0
σ_{cu_y}	yield strength [N/mm^2]	150.0
σ_{cu_t}	tensile strength [N/mm^2]	260.0
ν_{cu}	poison ratio	0.33
α_{cu}	coeff. of thermal expansion	$1.77{\cdot}10^{-5}$
Si-Fe (M400-50A)		
ρ_{fe}	density [kg/m^3]	7750.0
E_{fe_X}	modulus of elasticity X [kN/mm^2]	185.0
E_{fe_YZ}	modulus of elasticity Y,Z [kN/mm^2]	205.0
σ_{fe_yX}	yield strength X [N/mm^2]	310.0
σ_{fe_yYZ}	yield strength Y,Z [N/mm^2]	325.0
σ_{fe_tX}	tensile strength X [N/mm^2]	450.0
σ_{fe_tYZ}	tensile strength Y,Z [N/mm^2]	472.0
ν_{fe}	poison ratio	0.3
α_{fe}	coeff. of thermal expansion	$9.5{\cdot}10^{-6}$

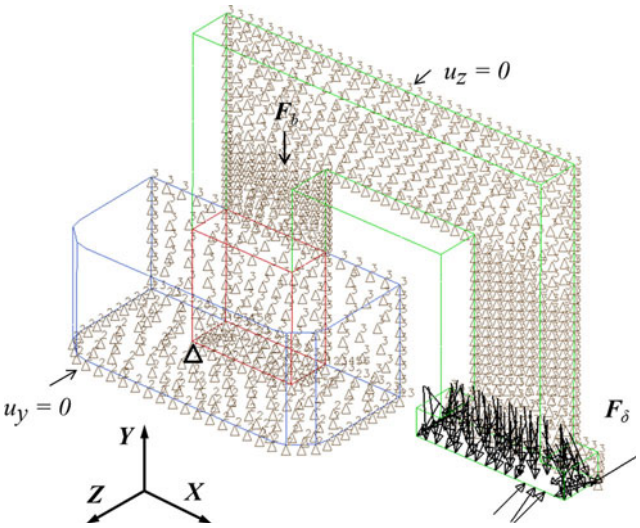

Fig. 9 Load case setup in *GENESIS* where (Δ) indicates SPCs, and F_δ and F_b the respective air-gap and body force vector fields

where E and σ represent the material constitutive matrix and the element stress matrix.

Two STR symmetry planes are defined. Translations in the Y and Z-directions are constrained in the XZ and XY symmetry planes, respectively. The model is anchored by single point constraints (SPCs) that restrict translation along the X-axis. The mapped air-gap (F_δ) and body (F_b) vector force fields are included as `FORCE` data deck entries. Only X and Y force components are applied to the air-gap nodes that fall in the XY symmetry plane. The model initial temperature is set to 20 °C, using the `TEMPD` data deck. Thermal stresses are derived from the nodal temperature distribution calculated in the thermal analysis (Section 4.2). Nodal temperatures are incorporated with the `TEMP` data deck. Temperature effects on material mechanical properties are ignored. The model weight is added by applying a gravitional acceleration ($g = -9.81\text{m/s}^2$) acting along the Y-axis. The total mass, nodal displacements, and von Mises element stresses are extracted.

5 Optimisation

The MDO problem formulation, which involves the coupling of the three disciplines, the feasibility checks, the normalisation of design variables and constraints, and the calculation of five random baseline designs, are presented next.

The high interdisciplinary coupling and the strong deterministic sequence (EM→TH→STR) of this MDO problem allows for the simplification of the conventional MDF (Martins and Lambe 2013) scheme. The MDO flow diagram in Fig. 10 presents the conventional MDF scheme and a compact version thereof.

The conventional MDF scheme involves no coupling variable consistency or analysis constraints at system level. Instead, coupling variable consistency is ensured at the MDA level. Here, the MDA calculations are looped until disciplinary state consistency is within a certain error tolerance. The compact MDF scheme differs in that the MDA feasibility loop is removed and replaced by the calculation of the sum of state consistency errors. This error sum is then managed as a system level optimisation constraint. Note that this compact MDF does not yield an AAO or IDF (Section 1) scheme, because the disciplinary FEAs are not executed at once and no estimated state consistency variables are included.

Of all the coupling variables (see Fig. 4), the system state is most sensitive to air-gap deformations $y_5(x)$. This allows for a simplified state consistency error calculation by only considering the convergence of the air-gap deformations. Figure 11 shows the normalised magnetic stress at the air-gap $y_3(x)$, the core Joule losses $y_1(x)$, and the average core temperatures $y_2(x)$ with respect to air-gap clearance variations. It is clear that the smaller the air-gap clearance, the larger the core magnetic flux density, the higher the iron losses, and the larger air-gap attraction forces. Note that the magnetic stress gradient increases dramatically for air-gap clearances smaller than 1 mm. The air-gap deformation consistency metric is applied in both MDF schemes.

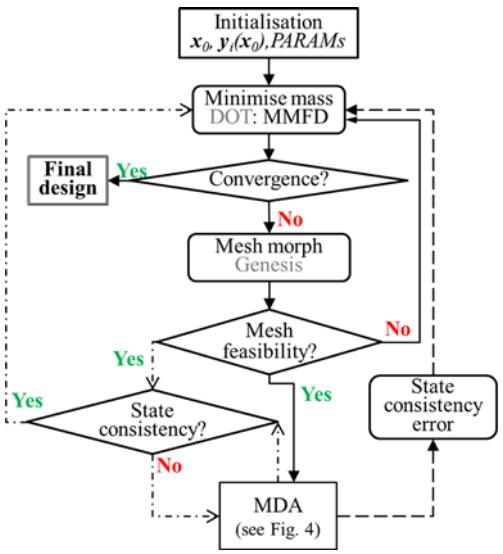

Fig. 10 The flow diagram shows the conventional MDF (– · –) and the compact MDF (– – –) schemes

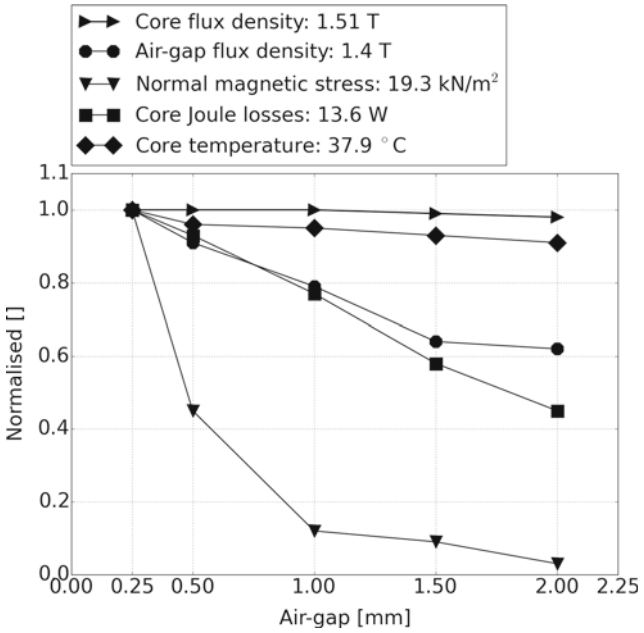

Fig. 11 Coupling variable sensitivities

The MDO problem considered, is expressed as

$$
\begin{aligned}
&\min_{x} \quad \text{mass}(x, y_i(x)), i = 1, \ldots, 5 \\
&\text{subject} \quad \text{to} \\
&\quad g_1(x, y_5(x)) = \frac{err(x, y_5(x)))}{tol} - 1.0 \leq 0 \\
&\quad g_2(x, y_4(x)) = \frac{\hat{J}(x, y_4(x)))}{J_n} - 1.0 \leq 0 \\
&\quad g_3(x, y_5(x)) = \frac{B_{\delta_{rms}}(x, y_5(x))}{B_{\delta\_n}} - 1.0 \leq 0 \\
&\quad g_4(x, y_5(x)) = \frac{\hat{B}_{core}(x, y_5(x))}{B_{core\_n}} - 1.0 \leq 0 \\
&\quad g_5(x, y_{1,2,4}(x)) = \frac{\tilde{T}_{core}(x, y_{1,2,4}(x))}{T_{core\_n}} - 1.0 \leq 0 \\
&\quad g_6(x, y_{1,2,4}(x)) = \frac{\tilde{T}_{coil}(x, y_{1,2,4}(x))}{T_{coil\_n}} - 1.0 \leq 0 \\
&\quad g_7(x, y_{2,3,5}(x)) = \frac{\tilde{\sigma}_{core}(x, y_{2,3,5}(x))}{\sigma_{core\_n}} - 1.0 \leq 0 \\
&\quad g_8(x, y_{2,3,5}(x)) = \frac{\tilde{\sigma}_{coil}(x, y_{2,3,5}(x))}{\sigma_{coil\_n}} - 1.0 \leq 0 \\
&\quad g_9(x) = \frac{dz_{core}(x)}{d_{min}} - 1.0 \leq 0 \\
&\quad g_{10}(x) = \frac{dy_t(x)}{h_{tooth}} - 1.0 \leq 0 \\
&\quad g_{11}(x) = \frac{dx_t(x)}{1.2 w_{core2}} - 1.0 \leq 0 \\
&\quad x = [\psi_{x6:7}, \psi_{x8:9:10}, \psi_{y1:2}, \psi_{y1:4:5}, \psi_{y3}, \psi_{y5}, \ldots \\
&\qquad \psi_{z3:8:9:10}, \psi_{z8:9:10}] \forall \psi \in [-1.0, 1.0]
\end{aligned}
\tag{33}
$$

where x, $y_i(x)$, and $g_j()$ are the normalised design variable vector, the coupling vectors in hierarchical order, and the normalised inequality constraints, respectively.

The normalisation of the design variables and the constraints are to ensure a well-conditioned problem. These constraints are functions of both the design vector and coupling variables. Note that the first constraint is only applicable in the compact MDF scheme. The design variable vector x only contains sets of morphing vectors. The applied linear morphing operation is discussed in Section 5.1.

The distribution and declaration of the coupling vector $y_i(x)$ variables are presented in Section 5.2. Constraint and the relevant normalisation values are defined in Section 5.3. This local optimisation problem is solved with the Modified Method of Feasible Directions (MMFD) algorithm. The local optimum is calculated by combining this gradient-based algorithm with a multi-start approach. Details of the multi-start approach are discussed in Section 5.4. The MMFD algorithm is one of the embedded options in the Design Optimisation Toolbox (*DOT*) code (Vanderplaats 2014). Default search and sensitivity parameters are applied. The coupling and handling of the disciplinary models and *DOT* are managed within a *Python* script.

5.1 Morphing

Linear mesh morphing was performed by using the *GENESIS* code. Morphing the mesh involves the selection of shape domains, the allocation of morph vectors, and element/mesh feasibility checks. Domains are associated with `BAR` elements of which the element lengths and orientations are confined to a selection of nodes. The design vector in (33) comprises of morph vector sets. A typical set, like $\psi_{x6:7}$, denotes vectors parallel to the x-axis assigned to morph Domains 6 and 7. The allocation of these domains and vectors are depicted in Fig. 12.

These vectors coincide with the `BAR` elements at specific `BAR` endpoints. All mesh domains are simultaneously morphed. This is followed by the calculation of the new nodal coordinates (i.e. $y_1(x)$) and model surface areas (i.e. $y_5(x)$). The mesh is updated by replacing the nodal coordinates

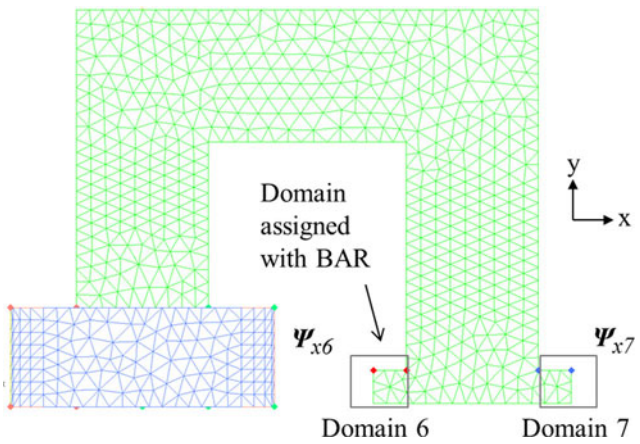

Fig. 12 Example of morph domain and morph vector allocations

of the previous MDA run with the newly calculated coordinates. This operation is performed in both MDF schemes before every MDA calculation. Therefore, for a fixed morph vector direction, the vector magnitude increases successively per iteration. This leads to the distortion of elements (mathematically) and the violation of FEA boundary conditions. Such issues can be mitigated by either limiting the morph vector magnitude or by adding an element quality check routine. In this study, the element quality and boundary feasibility are checked prior to MDA calculations (Fig. 10). Elements are checked by calling the `SHAPECK` parameter in *GENESIS*. Boundary conditions are conserved using geometry constraints i.e. $g_{9-11}(x)$. Additionally, the modification of discipline-specific element quality parameter specifications is also possible. Numerically, this allows the setting of the model/discipline fidelity level. In this study, the element quality parameters specific to the EM discipline are considered.

5.2 Disciplinary coupling

The hierarchical coupling of EM-TH, TH-STR, and EM-STR are shown in Fig. 13. The disciplinary coupling variable transferals are managed with a *Python* `dictionary` mapping data type (Python 2014). Typically, a dictionary entry consists of a key and a value pair which, in turn, may be a single vector or an array of vectors. Here, mapped nodal data is indexed using node `IDs` as keys, while the corresponding data (e.g. temperature) is included as scalar/vector arrays, e.g. `GRID['12']=[0.01,0.25,0.2]`. The disciplinary coupling and state variables are declared in Table 4.

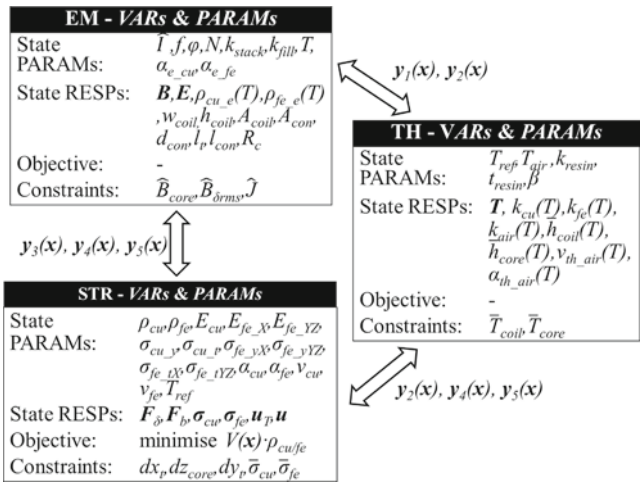

Fig. 13 MDA variable distribution; RESP - response

Table 4 Model state parameters and coupling variables

Symbol	Property [Unit]	Value/Eqn.
EM		
$\hat{I}$	supply current amplitude [A]	20.0
f	supply frequency [Hz]	50.0
φ	supply phase angle [°]	0.0
N	number of coil turns	48.0
k_{stack}	lamination stacking factor	0.98
k_{fill}	coil solidity factor	0.80
α_{cu_e}	coeff. resistivity copper	see Table 2
α_{fe_e}	coeff. resistivity iron	see Table 2
B	magnetic field [T]	(7)
E	electric field [V/m]	(8,11)
$\rho_{cu\_e}(T)$	resistivity of copper	(15)
$\rho_{fe\_e}(T)$	resistivity of copper	(15)
w_{coil}	coil-side width [mm]	see Fig. 6
h_{coil}	coil height [mm]	see Fig. 6
A_{coil}	coil-side area [mm^2]	(12)
A_{con}	conductor area [mm^2]	(12)
d_{con}	conductor diameter [mm]	(12)
l_t	coil turn length [mm]	(13)
l_{con}	avg. conductor length [mm]	(14)
R_c	coil resistance [Ohm]	(16)
TH		
T_{ref}	reference temperature [°C]	20.0
T_{air}	air temperature [°C]	20.0
k_{resin}	cond. of resin [W/m·°C]	0.26
t_{resin}	resin layer thickness [mm]	0.5
β	expansion coeff. of air [1/°C]	3.41·10^{-}3
T	nodal temperature field [°C]	(30)
$k_{cu}(T)$	cond. of copper [W/m·°C]	(18)
$k_{fe}(T)$	cond. of iron [W/m·°C]	(19)
$k_{air}(T)$	cond. of air [W/m·°C]	(20)
$\bar{h}_{coil}(T)$	conv. coeff. for coil [W/m^2·°C]	(23)
$\bar{h}_{core}(T)$	conv. coeff. for core [W/m^2·°C]	(23)
$\nu_{th\_air}(T)$	kinematic viscosity of air [m^2/s]	(27)
$\alpha_{th\_air}(T)$	thermal diffusivity of air [m^2/s]	(28)
STR		
State *PARAMs* are declared in Table 3		
F_δ	air-gap loads [N]	(31)
F_b	body loads [N]	(31)
σ_{cu}	stress distribution in copper	(32)
σ_{fe}	stress distribution in iron	(32)
u_T	thermal induced displacements	(32)
u	load induced displacements	(31)

5.3 Constraints

Normalised inequality constraints ($g_j(x)$) comprising discipline and system limitations are applied. The first constraint

Table 5 Constraint functions normalisation parameters

Symbol	Property [Unit]	Value
J_n	max. current density [A/mm^2]	3.0
B_{δ_n}	r.m.s air-gap flux density [T]	0.6
B_{core_n}	allowable core flux density [T]	1.2
T_{core_n}	max. core temperature [°C]	60.0
T_{coil_n}	max. coil temperature [°C]	100.0
σ_{core_n}	allowable core stress [N/mm^2]	200.0
σ_{coil_n}	allowable coil stress [N/mm^2]	150.0
d_{min}	allowable core depth [mm]	5.0
h_{tooth}	allowable tooth height [mm]	1.0
$1.2w_{core2}$	allowable tooth width [mm]	22.0

in (33) is a system state consistency constraint only applicable to the compact MDF scheme. In the conventional MDF scheme, this constraint is removed and embedded in the MDA block as a `while`-loop argument. In both cases, the maximum air-gap deformation is to limited to less than 0.01 mm. Functions $g_{2\rightarrow 8}$ are disciplinary constraints, whereas $g_{9\rightarrow 11}$ are system geometry constraints. The normalisation values for the constraint functions in (33) are specified in Table 5.

5.4 Baseline models

Five randomly selected initial designs were considered in the multi-start approach. These designs differ significantly in geometry (Fig. 14). Note that the geometry of both the yoke and the coil differs. The model dimensions with reference to Fig. 6, the corresponding constraint values, and the initial objective values are given in Table 6.

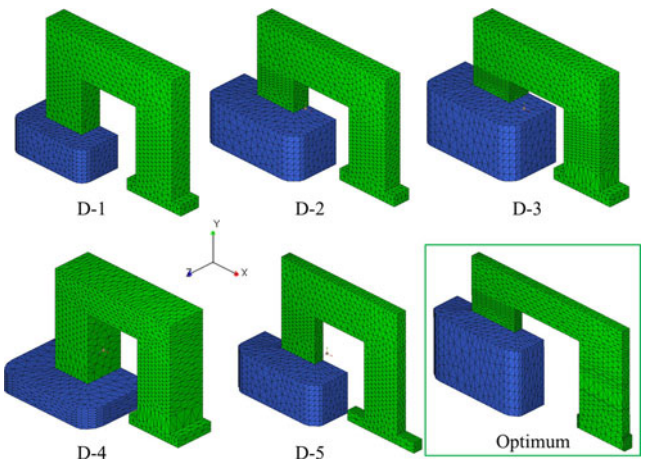

Fig. 14 Baseline designs and optimum design (in box)

Table 6 Constraint and objective function values for initial and optimum designs

Symbols	D-1	D-2	D-3	D-4	D-5	Opt.
Dimensions [mm]						
d_{con}	3.5	5.5	6.0	4.5	5.0	3.5
w_{coil}	10.0	15.0	15.0	18.0	15.0	10.0
d_{coil}	20.0	23.0	25.5	38.0	20.0	11.0
h_{coil}	15.0	20.0	25.0	10.0	20.0	19.1
h_{core1}	45.0	35.0	9.66	34.8	41.2	37.7
h_{core2}	54.5	49.5	49.5	39.3	37.7	51.3
h_{core3}	20.0	20.2	20.3	14.9	21.8	12.7
w_{core1}	70.0	70.0	70.0	70.0	70.0	70.0
w_{core2}	20.0	20.0	18.0	21.0	20.0	20.0
d_{core}	10.0	8.0	10.5	20.0	5.0	3.0
h_t	5.0	4.0	5.5	5.0	5.0	5.0
w_t	30.0	29.8	31.0	29.8	40.0	21.8
δ	1.0	1.0	1.0	1.0	1.0	1.0
Constraint function values						
g_1	-0.99	-0.99	-0.98	-0.99	-0.99	-0.99
g_2	0.69	-0.20	-0.40	0.28	-0.13	-0.07
g_3	0.02	0.06	0.01	0.00	0.36	-0.03
g_4	-0.01	-0.03	0.04	-0.06	-0.07	-0.39
g_5	-0.71	-0.74	-0.74	-0.72	-0.74	-0.49
g_6	-0.49	-0.55	-0.56	-0.52	-0.54	-0.88
g_7	-0.82	-0.96	-0.95	-0.96	-0.96	-0.71
g_8	0.41	-0.43	-0.57	0.15	-0.37	-0.88
g_9	-2.00	-1.02	-0.90	-0.42	0.00	-0.82
g_{10}	-1.50	-0.48	0.03	-2.46	-1.36	-1.52
g_{11}	-4.00	-4.00	-4.00	-4.00	-4.00	-3.96
Objective function values [kg]						
mass	0.315	0.346	0.461	0.598	0.286	0.160

6 Results

All optimisation runs were executed on a single desktop computer with a INTEL Core i7-4770 CPU clocking at 3.4 GHz, with 16 GB RAM supporting a 64-bit architecture. The averaged optimisation results are presented in the last column in Table 6. All constraints listed in (33) were satisfied.

The optimum design weighs about 0.160 kg and is shown in Fig. 14. Comparing this design against the initial designs, its clear that the gaps between coil and core are minimised. A comparison of the MDF scheme performances is presented in Table 7. The compact MDF scheme is more effective as it delivers comparative results in less computational time. Notably, the conventional MDF scheme required more MDA iterations per single objective function evaluation.

Table 7 Comparison of MDF schemes

Schemes	D-1	D-2	D-3	D-4	D-5
Compact MDF					
Obj. value [kg]	0.158	0.161	0.162	0.160	0.157
No. of MDA iterations	234	203	271	263	206
Run time [h]	199	173	231	224	176
Conventional MDF					
Obj. value [kg]	0.158	-	-	-	-
No. of MDA iterations	211	-	-	-	-
Run time [h]	316	-	-	-	-

On average, a MDA iteration took about 55 minutes of which, the EM and TH FEAs took about 54 minutes and 1 minute, respectively. The EM is the dominating discipline. The clearance between the coil top-side and the core cantilever arm is enforced by a geometric constraint. This constraint ensures that the coil magnetic flux leakage remains minimal. Furthermore, as expected, a decrease in the width of the tooth increased the air-gap flux density. The MDO limiting constraint is the air-gap magnetic flux density. Figures 15, 16, 17, 18, 19 show the magnetic flux density, the current density, the temperature, the Von Mises stress, and the displacement distributions, respectively. These contour values are comparable to the normalisation values specified in Table 5.

7 Discussion

In this section important MDO/MDA considerations are addressed. These include the mesh management strategy, the MDA disciplinary coupling and disciplinary sequence, the MDF schemes, and the multi-start approach.

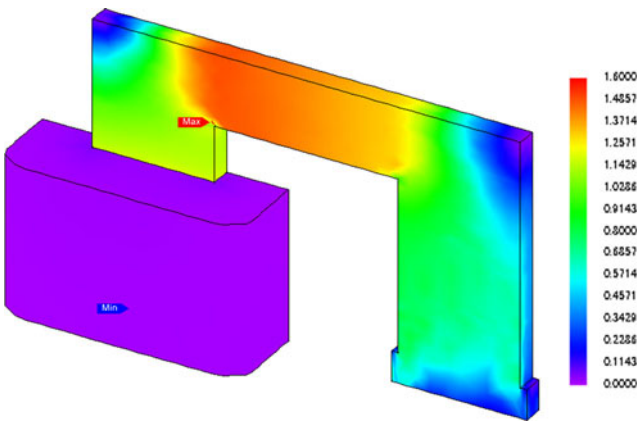

Fig. 15 Magnetic flux densities in [T]

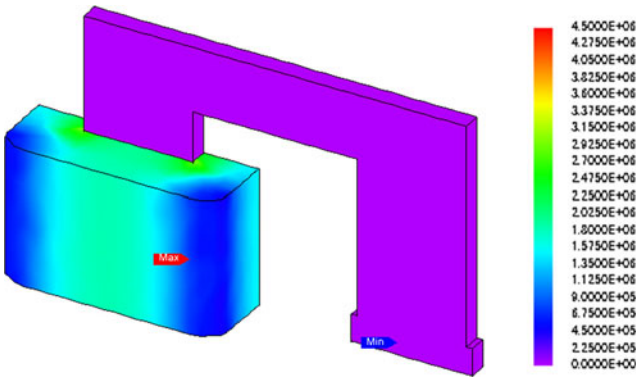

Fig. 16 Current densities in [A/m^2]

Starting with the MDA mesh management strategy, a remeshing or a morphing (single mesh) approach is possible. In applying the remeshing approach a new mesh is generated after either a single discipline analysis or a MDA; that is, a single mesh at system level or multiple meshes specific to the various disciplines. In this approach, the model mesh quality is conserved, but the mesh density is not.

Applying the morphing approach, a single mesh that satisfies all MDA requirements is generated. Here, the model mesh density is conserved but the mesh quality is not. This mesh may be partitioned to allow easy morph domain selection, localised mesh refinements, and disciplinary specific mesh refinements.

In addition, two linear morphing application methods are possible: the fixed vector magnitude and the fixed element quality methods. The former involves morphing vectors of fixed magnitudes for all MDA iterations. With the fixed element quality method, morphing vector magnitudes are varied during MDA iterations. Here, the range of variation is indirectly governed by a set of element quality properties that are verified during each MDA iteration. Comparing these morphing methods, the latter is more robust and requires fewer objective function evaluations.

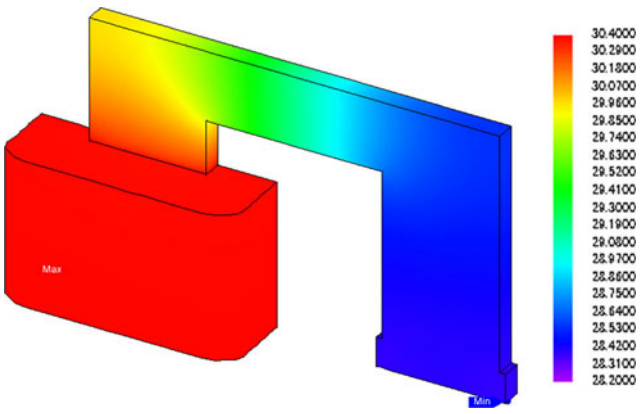

Fig. 17 Temperatures in [°C]

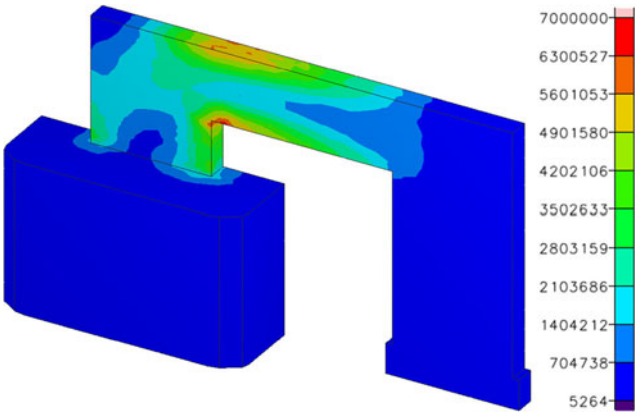

Fig. 18 Von Mises stresses in [N/m^2]

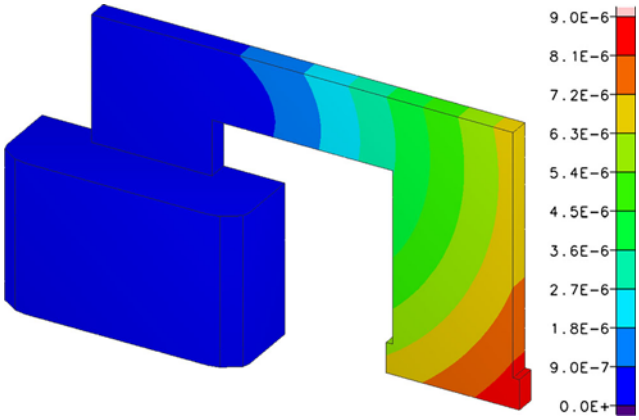

Fig. 19 Displacements in [m]

Furthermore, the morphing approach may be more applicable to MDO problems where the feasible design space is small, meaning the initial model is close to the optimum, or the problem comprises a large number of disciplines, as the large number of disciplinary constraints yields a smaller feasible design space. Here, the morphing vector magnitudes are governed by the mesh element dimensions and element type. That is, the smaller the characteristic element size the smaller the vector magnitudes, hence more optimisation iterations. A coarser mesh comprising hexahedral elements may yield a shorter solution time with a comparable accuracy. For all other MDO problems, remeshing that incorporates a mesh density check routine is recommended.

Problem properties that concern the MDA formulation are the degree of disciplinary coupling/interdependencies and disciplinary dominance. As a first approach, the degree of disciplinary coupling may be measured by the coupling variable to disciplinary state variable ratio. The degree of disciplinary coupling increases as this ratio approaches unity. In cases where the ratio equals unity, one may combine the relevant disciplines into a cluster in order to simplify the problem and to reduce computational expenses. In this study, the electromagnetic model is an example of such a cluster.

With reference to Section 4, the strong MDA hierarchical structure ensures the simulation stability needed for the formulation of the compact MDF scheme. This ranking is indicative of the existence of a dominating discipline. Disciplinary dominance in MDO problems may be more relevant if more than two disciplines are considered. A bi-discipline MDO problem may be seen as a system balancing exercise. For MDO problems of more than two disciplines, the coordination of the disciplinary FEAs needs to be determined. The MDA coordination/sequencing rule proposed and followed in this work involves the discipline specific time constants or energy conversion rates.

In a MDA setup, the disciplinary model with shortest time constant or highest energy conversion rate is analysed first, followed by the consecutive analyses of models with longer time constants.

The common time constant/frame selection is based on the longest time constant found in the MDA. The matching of disciplinary responses may be achieved by time-averaging operations or by FEA fidelity reductions (e.g. reduce to quasi-static). For example, the time constant of the electromagnetic response is shorter than that of the thermal and structural responses. From a MDO perspective, modelling the transient behaviour of the thermal and the structural subsystems will yield no improved design for the added computational expenses. Consequently, these subsystem models were reduced to quasi-static states of comparable time constants. The electromagnetic subsystem responses were time-averaged as to match the structural and thermal subsystem responses.

Another MDA coordination approach involves the asynchronous analyses of specific disciplinary models. Here, disciplinary models with long time constants or low energy conversion rates are analysed at different intervals or frequencies with respect to the dominating discipline. It may be described as the ”harmonic” layering of disciplinary analyses/responses within the MDA. The computational cost saved through the frequent exclusion of some models per MDA iteration may allow higher fidelity analyses across the entire system/problem. Consider this example; the small geometric alterations have a large affect of the magnetic flux density, but little impact on the thermal response of the core. Hence, the thermal model is only included and analysed during every, say, 5th MDA iteration.

When comparing the two MDF schemes applied in this study, the compact MDF scheme showed an additional design constraint which in effect reduced the feasible design space. Furthermore, the stability of this scheme may be ascribed to the weak coupling (or low interdependent sensitivity) between the disciplinary models considered. However, it is debatable whether this scheme is suitable

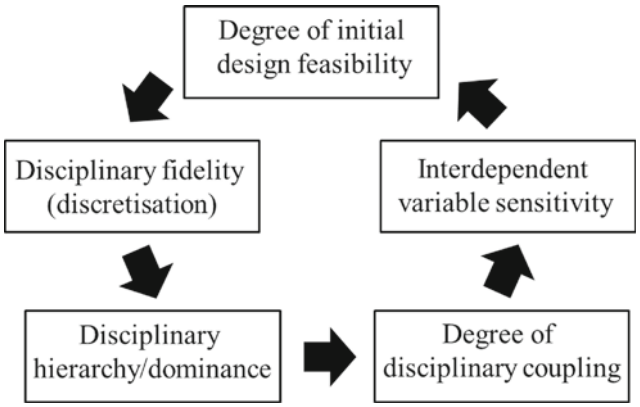

Fig. 20 MDO/MDA properties which need to be considered prior to modelling and problem decomposition

for strong coupled multidisciplinary systems such as FSI, MEMS, and photo-electromagnetic problems.

The multi-start approach can be applied by specifying different initial designs, as in this study, or by specifying different initial design vectors to a single initial design. However, in a MDO scheme the multi-start technique can be implemented differently. Instead of performing separate MDO operations for each initial design; these operations can be combined as parallel copies into a single MDO calculation; that is, a single MDO operation instead of multiple MDOs. This technique may also be extended to single-discipline global optimisation problems, where the use of monolithic MDO architectures in combination with gradient-based algorithms are applied.

Another multi-start related aspect concerns the degree of initial system feasibility. This concerns the feasibility of the individual sub-systems. In design space size, the infeasible region usually exceeds that of the feasible region. The degree of system feasibility may be defined as the reciprocal of the shortest spatial distance between the initial design point and the wholly feasible space. Of course, the highest degree is incurred when the initial design point falls within the fully feasible region. For example, the shorter the distance between initial design point and fully feasible region the higher the degree of system feasibility. Starting with an initial design of a low feasibility degree may incur unnecessary MDA iterations or worse it may lead to a lesser feasible design. It is therefore important to initiate the multi-start approach using designs of high degrees of feasibility.

In conclusion, formulating a full numeric MDO/MDA problem, one needs to consider numerous problem/system properties of which the most important are summarised in Fig. 20.

8 Conclusions

In this paper a high fidelity multidisciplinary design optimisation problem involving a electromagnetic-thermo-structural device was presented. The system comprised three disciplines that were numerically modelled and analysed using commercial codes. These models were based on a single mesh. A system mass minimisation, subjected to operational constraints, was performed. The design vector comprised the model morphing vectors. Two monolithic MDO architectures in combination with a multi-start algorithm were applied. A conventional and a new compact version of the multidisciplinary feasible decomposition scheme were considered and compared. The results indicated that solving the problem using the compact MDF is more efficient.

This problem is a suitable MDO benchmark, because it is reproducible, it consists of full numeric models, its fidelity level can be set, different mesh management strategies can be tested, disciplinary coupling strategies and sensitivities can be investigated, and different objectives can be specified.

A number of MDO/MDA setup considerations specific to full numeric problems were also presented. These concerned the MDA mesh management, the MDA disciplinary coupling and disciplinary sequence, the MDF schemes, and the multi-start approach. The conclusion is that there is no single mesh management strategy, decomposition scheme, or optimisation algorithm suitable for all types MDO problems. MDO is a problem specific operation.

Acknowledgments The author would like to thank the following individuals for their assistance: Phani Adduri of Vanderplaats Research and Development, Didier Zefack, and Yves Thioliere of POWERSYS Solutions. This research was funded by GreenFund which is a Development Bank of Southern Africa initiative. The grant number is RW1/1035.

References

Alexandrov N, Lewis R (2002) Analytical and computational aspects of collaborative optimization for multidisciplinary design. AIAA J 40:301–309. doi:10.2514/2.1646

Ammar I, Gerbaud L, Marin PR, Wurtz F (2005) Co-sizing of an electromechanical device by using optimisation process. COMPEL - Int J Comput Math Electr Electron Engx 24(3):997–1012. doi:10.1108/03321640510598292

Amrhein M, O'Connell T, Wells J (2013) An integrated design process for optimized high-performance electrical machines. In: Electric Machines Drives Conference (IEMDC), 2013 IEEE International, pp 847–854. doi:10.1109/IEMDC.2013.6556197

Balling R, Wilkinson C (1997) Execution of multidisciplinary design optimization approaches on common test problems. AIAA J 35(1):178–186. doi:10.2514/2.7431

Cheng-Ju W, Shih-Yu L, Shang-Chin C, Chia-Yun T, Jia-Yush Y (2014) Temperature effects on the magnetic properties of silicon-steel sheets using standardized toroidal frame. Sci World J 2014(975051). doi:10.1155/2014/975051

Cox S, Haftka R, Baker C, Grossman B, Mason W, Watson L (2001) A comparison of global optimization methods for the design of a high-speed civil transport. J Global Optim 21(4):415–432. doi:10.1023/A:1012782825166

Cramer E, Dennis J Jr, Frank P, Lewis R, Shubin G (1994) Problem formulation for multidisciplinary optimization. SIAM J Optim 4(4):754–776. doi:10.1137/0804044

Cros J, Viarouge P, Kakhki M (2011) Design and optimization of soft magnetic composite machines with finite element methods. IEEE Trans Magn 47(10):4384–4390. doi:10.1109/TMAG.2011.2157113

Floudas C, Gounaris C (2009) A review of recent advances in global optimization. J Global Optim 45(1):3–38. doi:10.1007/s10898-008-9332-8

Fouskakis D, Draper D (2007) Stochastic optimization: a review. Int Stat Rev 70(3):315–349. doi:10.1111/j.1751-5823.2002.tb00174.x

Hammadi M, Choley J, Penas O, Riviere A (2012) Multidisciplinary approach for modelling and optimization of road electric vehicles in conceptual design level. In: Electrical Systems for Aircraft, Railway and Ship Propulsion (ESARS), pp 1–6. doi:10.1109/ESARS.2012.6387488

Incropera F, DeWitt D (2002) Fundamentals of Heat and Mass Transfer, 5th. Wiley

Keysan O, McDonald A, Mueller M (2011) A direct drive permanent magnet generator design for a tidal current turbine(seagen). In: Electric Machines Drives Conference (IEMDC), 2011 IEEE International, pp 224–229. doi:10.1109/IEMDC.2011.5994850

Kreuawan S, Gillon F, Brochet P (2008) Optimal design of permanent magnet motor using multidisciplinary design optimization. In: Electrical Machines, 2008. ICEM 2008. 18th International Conference on, pp 1–6. doi:10.1109/ICELMACH.2008.4800108

Lasdon L (2002) Optimization theory for large systems. Dover Publications Inc.

Martins J, Lambe A (2013) Multi-disciplinary design optimization - a survey of architectures. AIAA J 51(9):2049–2075. doi:10.2514/1.J051895

Miyagi D, Aoki Y, Nakano M, Takahashi N (2010) Effect of compressive stress in thickness direction on iron losses of nonoriented electrical steel sheet. IEEE Trans Magn 46(6):2040–2043. doi:10.1109/TMAG.2010.2042691

Mukundan S (2003) Structural design and analysis of a lightweight composite sandwich space radiator material. Master's thesis, Texas A&M University

Pinchuk A, Silvester P (1985) Error estimation for automatic adaptive finite element mesh generation. IEEE Trans Magn 21(6):2551–2554. doi:10.1109/TMAG.1985.1064147

Pyrhönen J, Jokinen T, Hrabovcová (Wiley) Design of Rotating Electrical Machines

Python (2014) Section 5.8- Mapping Types - *dict*., URL http://docs.python.org/2.7/

Sobieszczanski-Sobieski J (1989) Optimisation by decomposition - a step from hierarchic to non-hierarchic systems. Recent Adv Multidiscip Anal Optim 1:51–78

Takahashi N, Miyagi D (2011) Effect of stress on iron loss of motor core. In: Electric Machines Drives Conference (IEMDC), 2011 IEEE International, pp 469–474. doi:10.1109/IEMDC.2011.5994642

Takahashi N, Morishita M, Miyagi D, Nakano M (2010) Examination of magnetic properties of magnetic materials at high temperature using a ring specimen. IEEE Trans Magn 46(2):548–551. doi:10.1109/TMAG.2009.2033122

JMAG (2014) JMAG - Simulation technology for electromechanical design., URL http://www.jmag-international.com/

Tosserams S, Etman L, Rooda J (2010) A micro-accelerometer mdo benchmark problem. Struct Multidiscip Optim 41(2):255–275. doi:10.1007/s00158-009-0422-0

Vanderplaats (2014) Vanderplaats Research and Development - Genesis., URL http://www.vrand.com/genesis.html

Venter G (2010) Review of Optimization Techniques, John Wiley and Sons, Ltd. doi:10.1002/9780470686652.eae495

Vinkó T, Izzo D (2011) Global optimisation heuristics and test problems for preliminary spacecraft trajectory design. Technical Report ACT-TNT-INF-2008-GOHTPPSTD, European Space Agency (ESA)